Supplementary information

Coseismic folding during ramp failure in the Sulaiman thrust belt

Muhammad Tahir Javed, Sylvain Barbot, Farhan Javed, Carla Braitenberg, and Aamir Ali

Contents of the file

- **Figure S8:** RMS L-curves for forward- and backward-vergent fault-bend fold and fault-propagation fold structures

Introduction

This supporting information provides a detailed description of the methodology used for InSAR data processing and Bayesian inversion (Text S1), supported by Figures S1 to S6, and Tables S1 to S3. Text S2, Figures S7, S8, and Tables S3 to S6 support the main text of section 2, describing geometry of the kinematic inversions of FBF, and FPF models and determination of the distribution of the coseismic slip. Text S3 defines the potency density, in support of section 2 of the main text.

Text S1

1 Methods of InSAR processing and modeling

1.1 InSAR anlysis

We select two pairs of Sentinel-1A observations of ascending track $T-071$ and descending track $T-005$ in TOPS mode that have the shortest perpendicular and temporal baselines with the least seasonal atmospheric variation to retain high correlation. Features of these datasets including orbit number, track, incidence angle and heading angle of ascending and descending tracks are given in Table S1. We generate the ascending and descending interferograms using single look complex (SLC) products through the GMT5SAR code (Sandwell et al., 2011). We mostly follow the default procedure for processing and filtering. We use the amplitude image and a 1-arc-second SRTM digital elevation model (Farr & Kobrick, 2000) for co-registration and to produce the topographic phase correction. We generate the unwrapped interferometric phase for the ascending and descending acquisitions. We improve the coregistration through 1) geometric alignment on the basis of precise orbit (Sansosti et al., 2006), 2) de-ramping of SLC before interpolation of data (Miranda et al., 2015) and 3) mitigation of mis-registration on the basis of the spectral technique (Prats-Iraola et al., 2012). Azimuth coregistration is more difficult in TOPS mode acquisition than conventional strip map (De Zan & Monti Guarnieri, 2006). After high-quality co-registration, we remove the effect of topography from the SAR interferogram. In the first stage, we use a Gaussian filter with a wavelength of 200 m, and in the second a Goldstein filter is applied to the interferograms (Goldstein & Werner, 1998; Baran et al., 2003). We use SNAPHU (Chen & Zebker, 2002) to unwrap the interferogram with the threshold coherence of 0.15. Each subswath of interferometric SAR acquisition is processed individually and independently within its corresponding coordinates. In the end, geocoding is applied to transfer the radar coordinate system to the geographic coordinate system.

With the aim to define the data region to consider in the inversion, we have made a simulation of the expected surface deformation signal for a single fault, assuming an average dislocation. The deformation is shown in Figure S1. We take similar parameters as those inverted from the geodetic Bayesian inversion approach (length:16 km, width: 2.8 km, dip: 40 degrees, strike: 194 degrees, depth: 6.6 km, average slip: 28 cm). We find the signal to be confined to a region of 0.2° × 0.2° and to decay quickly from its central part, with a noise level of about 2 mm. This region limits the square of useful data since at greater distances we cannot expect to have any signal in the data, but just add data with noise or with a signal which has nothing to do with the earthquake. The topography of the deformed region is flat, which is a favorable situation in relation to atmospheric effects since they are correlated with topography. Nonetheless, we have tested also the interferograms on a wider region (0.6° × 0.6°) taking acquisitions before and after the 2015 Dajal earthquake, as shown in Figure S2. The figure clearly shows the presence of atmospheric noise to the west of the Dajal earthquake deformation zone (Figure S2a-e), although we had applied the Generic Atmospheric Correction Online Service (GACOS)for InSAR (Yu et al., 2018) and removed atmospheric noise. We find significant noise on the western side of the coseismic deformation zone in the interferograms of 10 November to 17 October 2015 (Figure S2a). This noise signal is absent in the descending interferogram from 01 October to 18 November 2015 (Figure S2f), which demonstrates that the western signal on LOS on the ascending interferogram is due to noise. Moreover, the noise is lower in the ascending track for the 10 November to 04 December 2015 interferogram (Figure S2e). This shows, the noise is probably due to local strong rains that affect the area in fall and is stronger where the topography rises steeply, which is to the western side of the deformation zone. We can clearly observe the region outside 0.2° x 0.2° area is noisy and can reach up to 15-20 cm. The inclusion of this wider area has a significant impact on the results, as the noise level is higher than the signal at those distances. We perform inversions for the wider region on the GACOS corrected data and find the posterior probability density (PDF) is not well converging, as shown in (Figure S5). The uncertainty on the inversion with the wider area is high. This confirms that our selected smaller region (black rectangle in Figure S2) is quite feasible for inversions and avoids any unnecessary contribution of noise in the results.

1.2 Error Estimation

Variance and covariance of the datasets are generally estimated experimentally to characterize the InSAR data errors that have occurred due to phase decorrelation. The InSAR errors arise mainly due to varying ionosphere and water vapor content in the upper atmosphere and lower atmosphere respectively (Hanssen et al., 1999). The error can also be encountered due to steep topographic variations at the site and anisotropic spatial variability (Knospe & Jonsson, 2010). We estimate the spatial variability of both ascending and descending interferograms using a semi-variogram (Wackernagel, 2003) by measuring the dissimilarity. We use the unbounded exponential function to compute dissimilarities with nugget, sill, and range variances for the ascending and descending interferograms separately (Table S2). Subsampled points used for Bayesian inversion for both interferograms are shown in Figure S3b, d respectively.

1.3 InSAR Modeling

We apply the geodetic Bayesian inversion (GBIS) approach (Bagnardi & Hooper, 2018) to the ascending and descending space-borne SAR interferograms covering the 2015 Dajal earthquake (Table S1). After estimating the experimental semivariogram by masking out the deformation zone, we use full-resolution InSAR data and then subsample both ascending (number of subsamples: 238) and descending (number of subsamples: 178) interferograms based on an adaptive quadtree gradient-based algorithm (Simons et al., 2002; Jonsson & Eklundh, 2002) using a threshold variance as given in Table S2. The large dataset is commonly subsampled in the Bayesian inversion to reduce the large computation time, and achieve enough information for a successful inversion (Bagnardi & Hooper, 2018). We prefer the gradient-based algorithm because the density of the samples is directly proportional to the displacement gradient and it recursively divides the LOS displacement into further four polygons each time, unless it achieves the selected threshold variance for ascending ($1.0 \times 10^{-2} mm^2$) and descending ($4.5 \times 10^{-3} mm^2$) interferograms (Figure S3a, c). We generate a kinematic synthetic model for a uniform rectangular dislocation source (Okada, 1992). The ascending and descending interferograms show the surface deformation of approximately 45 and 50 mm along their respective LOS direction (Figure S4a, b). Synthetic models (Figure S4c, d) with a single fault patch agree well with InSAR observed data, with average residuals of the order of average 2.3 mm for both interferograms (Figure S4e, f). We efficiently categorize the posterior probability density (PDF) of the ruptured fault geometry of the 2015 Dajal earthquake with automatic step size using the Metropolis-Hastings algorithm and the Monte Carlo Markov chain method (Tarantola, 2005; Fukuda & Johnson, 2008; Hastings, 1970;

Metropolis et al., 1953; Wang et al., 2017). We use 10^6 iterations to define posterior PDF, discarding the first 20,000 samples. We have used the epicentral location from seismic waveform modeling retrieved from the US Geological Survey (USGS, 2020), and ISC (International Seismological Centre) (Lentas et al., 2019) database as prior information. The inversion is done on both the wider area of $0.6^\circ \times 0.6^\circ$, which extends beyond the central earthquake deformation zone, and the smaller area of $0.2^\circ \times 0.2^\circ$ (Figure S2). As discussed in section 1.1 the wider area is significantly affected by the atmospheric noise accentuated westwards of the epicenter (Figure S2d). The posterior probability distribution for the wider area with 95% confidence intervals inversion results is given in Figure S5, for the smaller area in Figure S6. The noise in the wider area propagates into a greater uncertainty level and misfit in the results, for which reason this solution is discarded. The final ruptured fault geometry of the 2015 Dajal earthquake with the 95% confidence interval is given by fault dip ($40^\circ \pm 12$), strike ($194^\circ \pm 6$), length (14.7 km ± 2.8), width (2.9 km ± 1.2), and depth (6.5 km ± 1.2) (Table S3). We use 10^6 iterations to define posterior PDF, discarding the first 20,000 samples (Figure S6). We have also used the epicentral location from seismic waveform modeling retrieved from the USGS NEIC database as prior information. The calculated source fault geometry is given in Table S3.

Text S2

2 Kinematic Inversions and Folding

2.1 Geometry of FBF and FPF models

In FBF and FPF models, the geometry of the active axial surfaces is obtained assuming the conservation of layer thickness, length, and cross-sectional area of the incoming sediment in a balanced cross-section (Suppe, 1983; Suppe & Medwedeff, 1990). Assuming no cut-off angle between the incoming thrust sheet and the basal décollement for the FBF model (Figure 2a, see main text), the axial surface must bisect the décollement-ramp system, resulting in an angle of 70° clockwise for the deeper décollement, and 110° anti-clockwise for the shallower décollement (Figure 2b, see main text). For the FPF(Figure 2c, see main text), the axial surface 1 bisects the ramp-décollement with 70°, the axial surfaces 3 and 4 bisect the wedge above the top of the fold at 55° and 70°, respectively, whereas axial surface 2 bisects the frontal fold with 55° (Figure 2d, see main text). We consider V_1, V_3, the long-term slip-rate above and below the fault (dark line), and V_2 is the long-term slip-rate along the active axial surface (Figure 2a,b, see main text). The angle between V_1 and V_3 is 40°, V_1 and V_2 is 70° forms the closed hodograph shown as an inset in the (Figure 2b, see main text). The hodograph of the axial surface 2 is the same, but with a reversed sense of slip rates (Sathiakumar et al., 2020). The motion along the two top-fold axial surfaces 3, and 4 is explained by the closed hodographs (Figure 2d, see main text). V_2 is the long-term motion of the rocks in wedge above the two top-fold axial surfaces parallel to the passive axial surface – connects the dipping ramp and the two top-fold axial surfaces – at an angle of 82.5° from the horizontal. V_4 is -41.25° from the axial surface 4, and $V_3 = 83.5°$ from axial surface 3 forms the tow closed hodographs at axial surface 4, 3 respectively (Figure 2d, see main text). We also consider alternative models with the conjugate dip direction for the ramp with a similar structure but the opposite sense of motion.

Text S3

3 Potency density of the Dajal earthquake

The potency density — the average change of strain around the earthquake, i.e., the stress drop divided by the rigidity of the country rocks — is 44 micro-strain, comparable with that of the 2013 Mw 7.7 Balochistan, Pakistan earthquake, which had a similar centroid depth, and consistent with the general trend of potency density of thrust earthquakes worldwide (Nanjundiah et al., 2020)

Table S1: Features of Sentinel-1A interferometric pairs

Image pair (yy/mm/dd)	Track	Perpendicular baseline (m)	Temporal baseline (days)	Incidence angle (°)	Heading platform (°)
2015/10/17 – 2015/11/10	$ASC-T071$	174	24	$36-39$	-12.59
2015/10/01 – 2015/11/18	$DSC-T005$	40	48	$36-39$	-167.35

Table S2: Detail of interferogram errors calculated using semi-variogram

Track	Sill $(mm)^2$	Nugget $(mm)^2$	Range (km)	Threshold $(mm)^2$	Subsample (points)
$ASC-T071$	0.12	1.4×10^{-4}	9.75	1.0×10^{-2}	238
$DSC-T005$	0.038	2.3×10^{-3}	12.07	4.5×10^{-2}	178

Table S3: The estimated source fault parameters, inverting both ascending and descending interferograms along with their uncertainties by assuming single fault plane and ignoring fault-bends

Model	Lon (°)	Lat (°)	Str (°)	Dip (°)	Rake (°)	L (km)	W (km)	Dep (km)	Slip (m)	Mo ($10^{17}Nm$)	Mw
USGS	70.326	29.638	194	30	70	-	-	15.5	-	3.096	5.59
	-	-	182	47	68	-	-	11.0	-	1.792	5.44
GCMT	-	-	186	41	56	-	-	12.0	-	3.471	5.63
ISC	70.353	29.618	192	46	45	-	-	19.8	-	-	5.5
InSAR	70.28± 0.03	29.66± 0.02	194± 6	40± 12	79± 10	14.7± 2.8	2.9 ± 1.2	6.5 ± 1.2	0.28± 0.14	3.94 ± 4.0	5.66± 0.30

Table S4: The FPF and FBF models with varying dips at 7.5 km depth and their corresponding residuals. The 40° dip results consistently with the lowest RMS residuals.

Dip (°)	Forward-vergent FPF (mm)	Forward-vergent FBF (mm)	Backward-vergent FPF (mm)	Backward-vergent FBF (mm)
30	3.06	2.91	3.27	2.90
40	2.59	2.80	2.72	2.86
50	3.06	2.76	2.80	2.92

Table S5: AIC, RMS and Reduced-Chi-square analysis for forward- and backward-vergent models, depth = 7.5 km, dip = 40°. The reduced-chi-square statistic is a measure of the squared difference between the observed and modeled values, considering the degrees of freedom, and the sample size

Models	N	Np	RSS (mm^2)	RMS (mm)	AIC	Reduced-Chi Square
Forward-vergent FPF	17331	675	0.1246	2.59	2707.64	0.720
Forward-vergent FBF	17331	675	0.1401	2.80	2708.52	0.820
Backward-vergent FPF	17331	675	0.1285	2.72	2708.04	0.725
Backward-vergent FBF	17331	675	0.1429	2.86	2708.88	0.792

FBF: Fault Bend Fold

FPF: Fault Propagation Fold

N: InSAR data points

Np: Model parameters

RSS: Residual sum of square

RMS: Root mean square

AIC: Akaike Information Criterion

Table S6: AIC, RMS for forward- vergent FPF model with dip = 40°with, and varying depth.

Depth (km)	N	Np	RSS (mm^2)	RMS (mm)	AIC
6.0	17331	675	0.2009	3.40	2712.57
7.5	17331	675	0.1227	2.59	2707.64
9.0	17331	750	0.1095	2.51	3006.92
10.5	17331	900	0.1022	2.42	3606.59

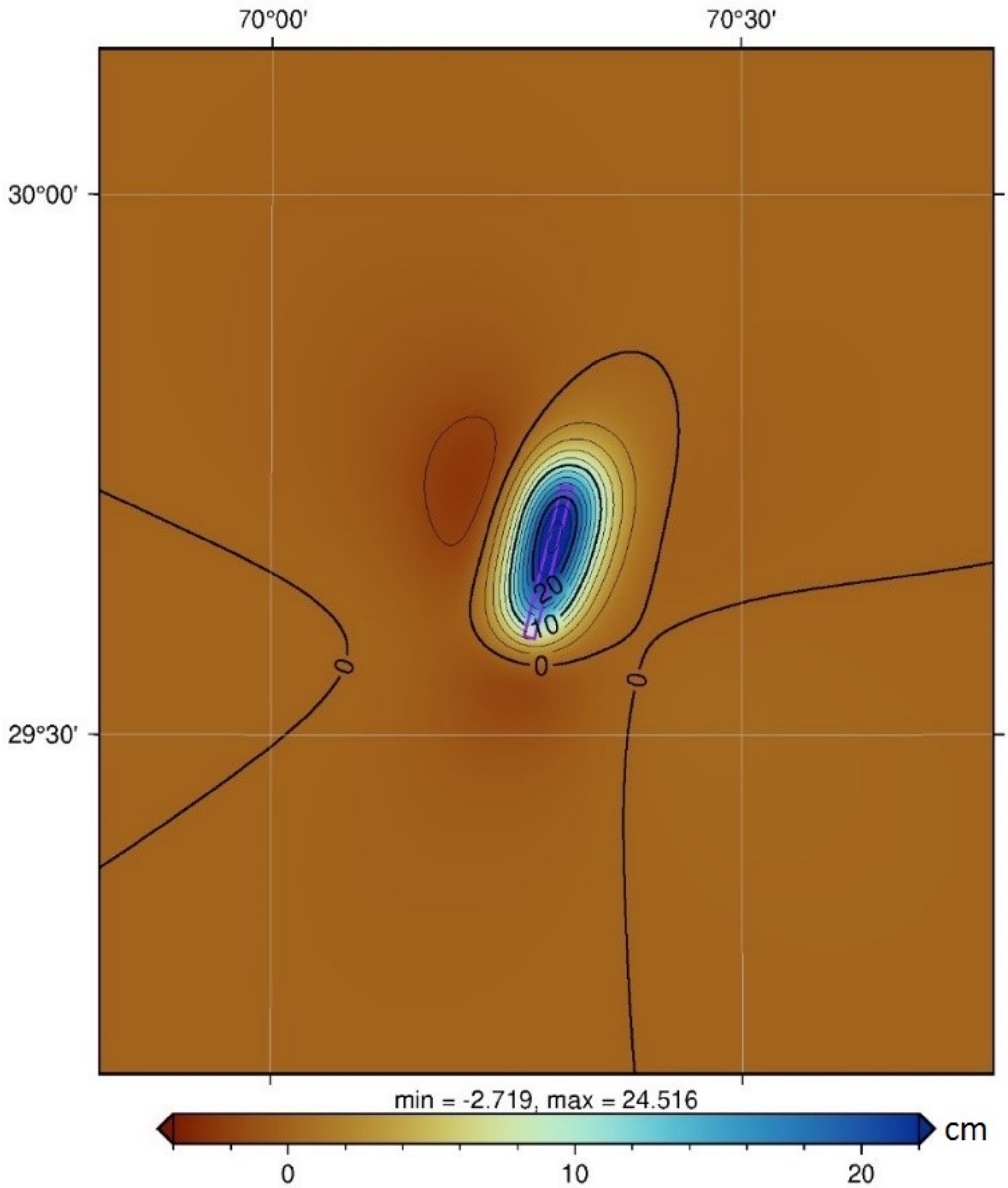

Figure S1: The simulation of the expected surface deformation signal for a single fault, assuming an average dislocation using the inverted fault parameters estimated from Bayesian inversion approach

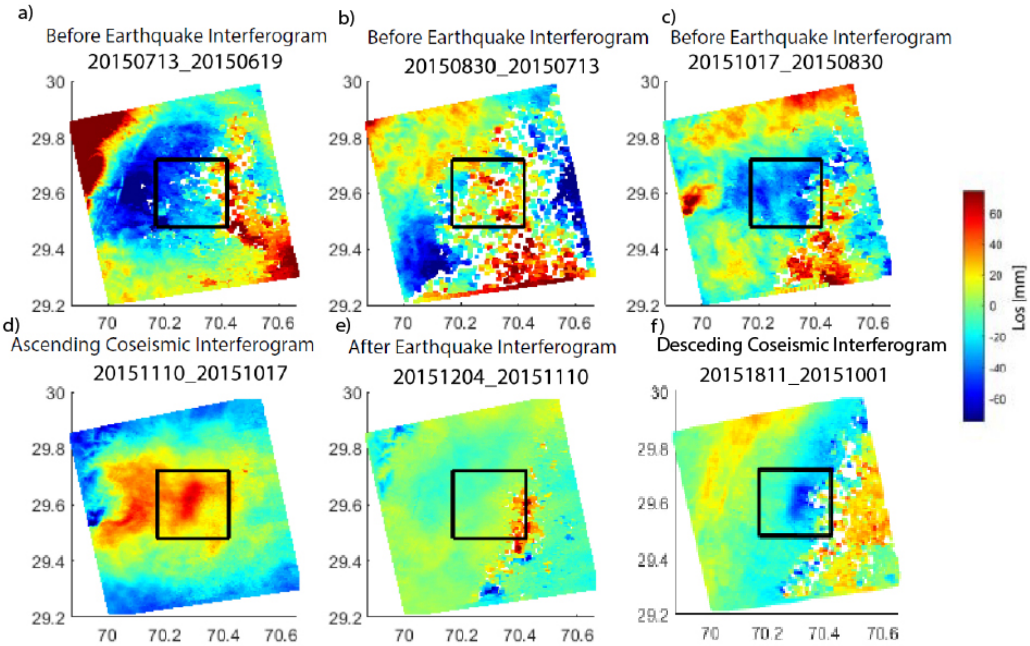

Figure S2: LOS displacement for ascending (a-e), and descending (f), calculated using Sentinel-1A interferograms for time couples before, after, and across the 2015 Dajal earthquake of 23 October 2015.

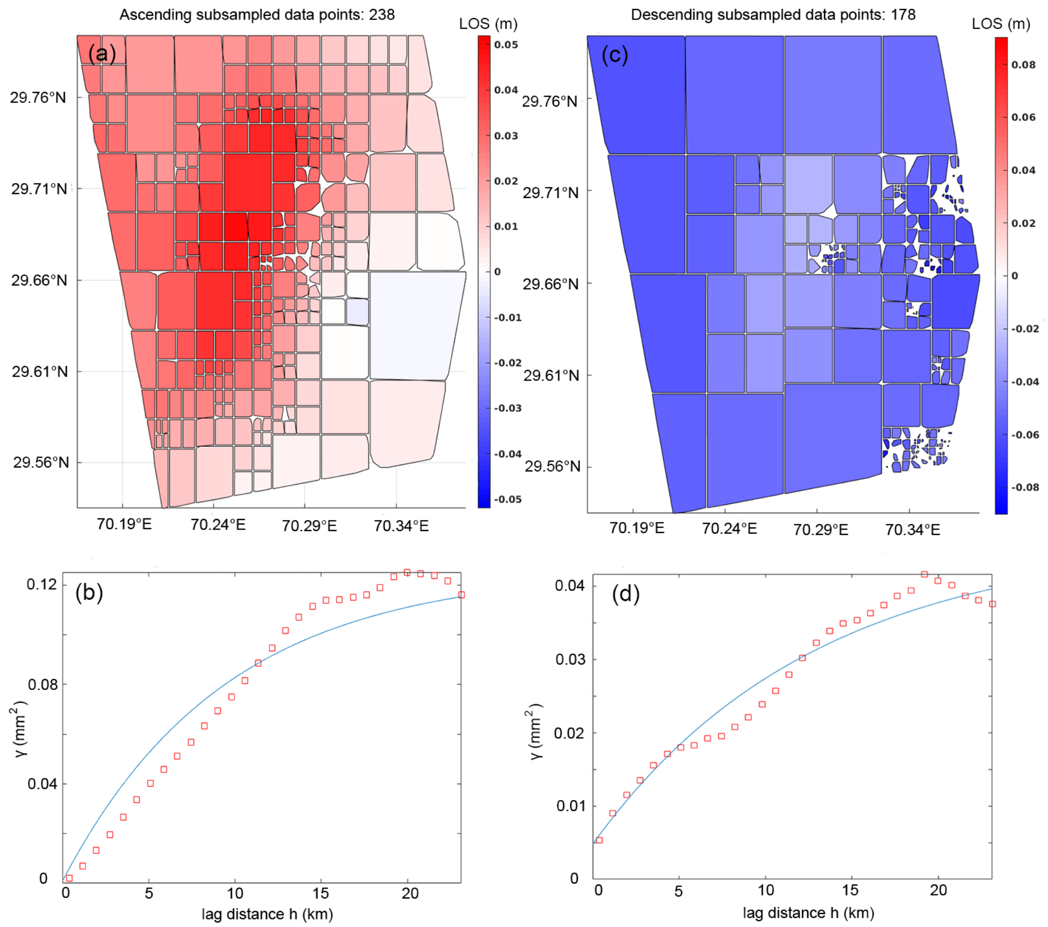

Figure S3: The adaptive quadtree gradient-based subsampling and semi-variogram analysis. a, b) The subsampling and semi-variogram to estimate the covariance of the processed interferogram during ascending track respectively. The ascending interferogram is subdivided into 238 points with the threshold phase variance of 1.0×10^{-2} mm^2. c, d) The subsampling and semi-variogram to estimate the covariance of the processed interferogram during descending track respectively. The descending interferogram is subdivided into 178 points with the threshold phase variance of 4.5×10^{-2} mm^2. Blue (solid lines) is the exponential function of the semivariogram while Red (blocks) is the experimental semivariogram. The local origin for both interferograms is 70.289°N and 29.662°E.

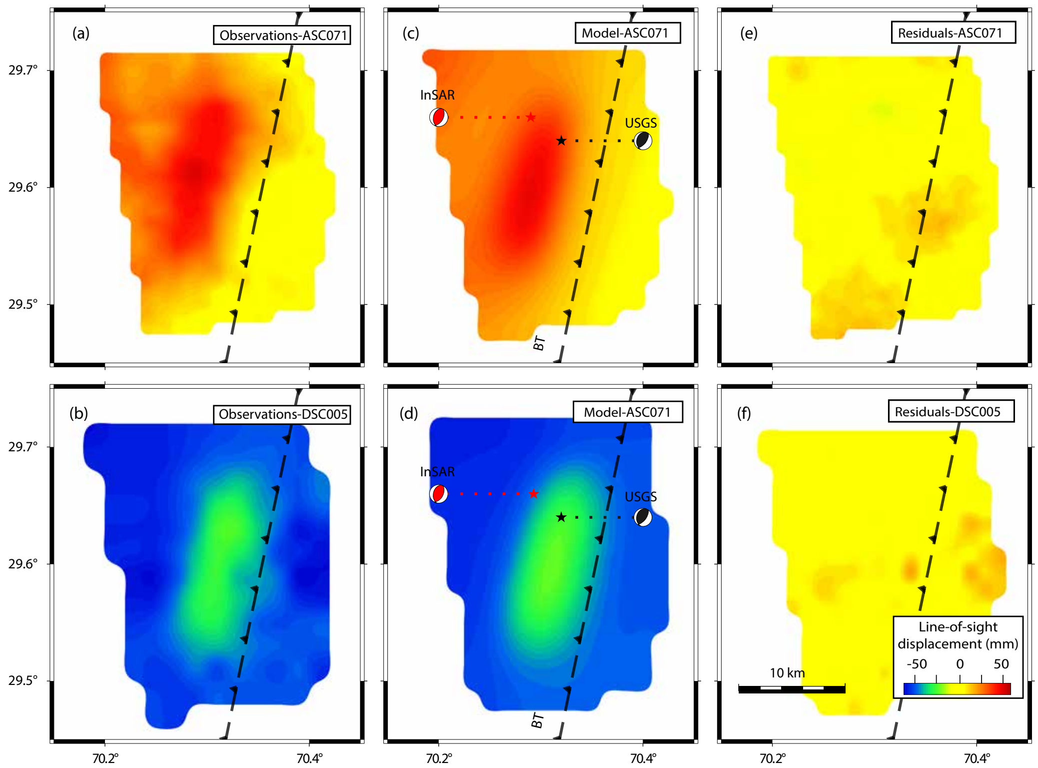

Figure S4: Single fault plane solution by using GBIS approach a, b) observation, c, d) synthetic interferogram and e, f) residual of the ascending track (T071) and descending track (T005) respectively. The deformation along the LOS displacement is approximately 50 mm and 45 mm along with less than 2.3 mm residual for descending and ascending track respectively. The focal mechanism solution (red colored) is produced by using inverted ruptured fault parameters and the focal mechanism solution (black colored) is taken from USGS.

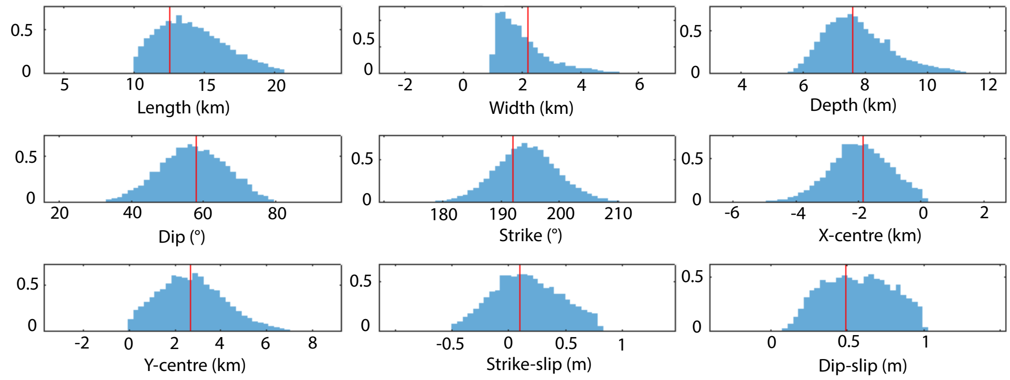

Figure S5: Histograms of source fault model parameters through Bayesian inversion approach with 10^6 samples, on wider area of 0.6° x 0.6°. The y-axis represents the probability density, and the red line indicates the optimal model values with 95% confidence interval for GACOS corrected data. (Rejected solution).

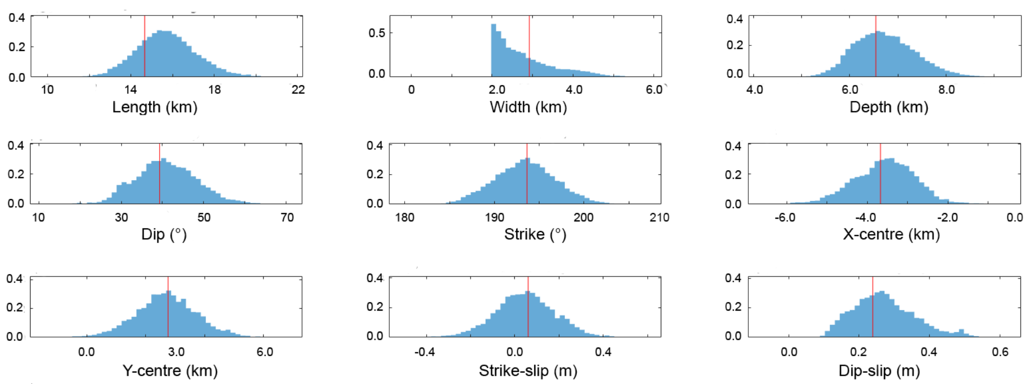

Figure S6: Histograms of source fault model parameters through Bayesian inversion approach with 10^6 samples, on area of 0.2° x 0.2°. The y-axis represents the probability density, and the red line indicates the optimal model values with 95% confidence interval. The optimal model has fault length around 15 km, width 2.9 km, depth 6.5 km, dip 40°, strike 194°, and average slip 0.28 m. (Best solution).

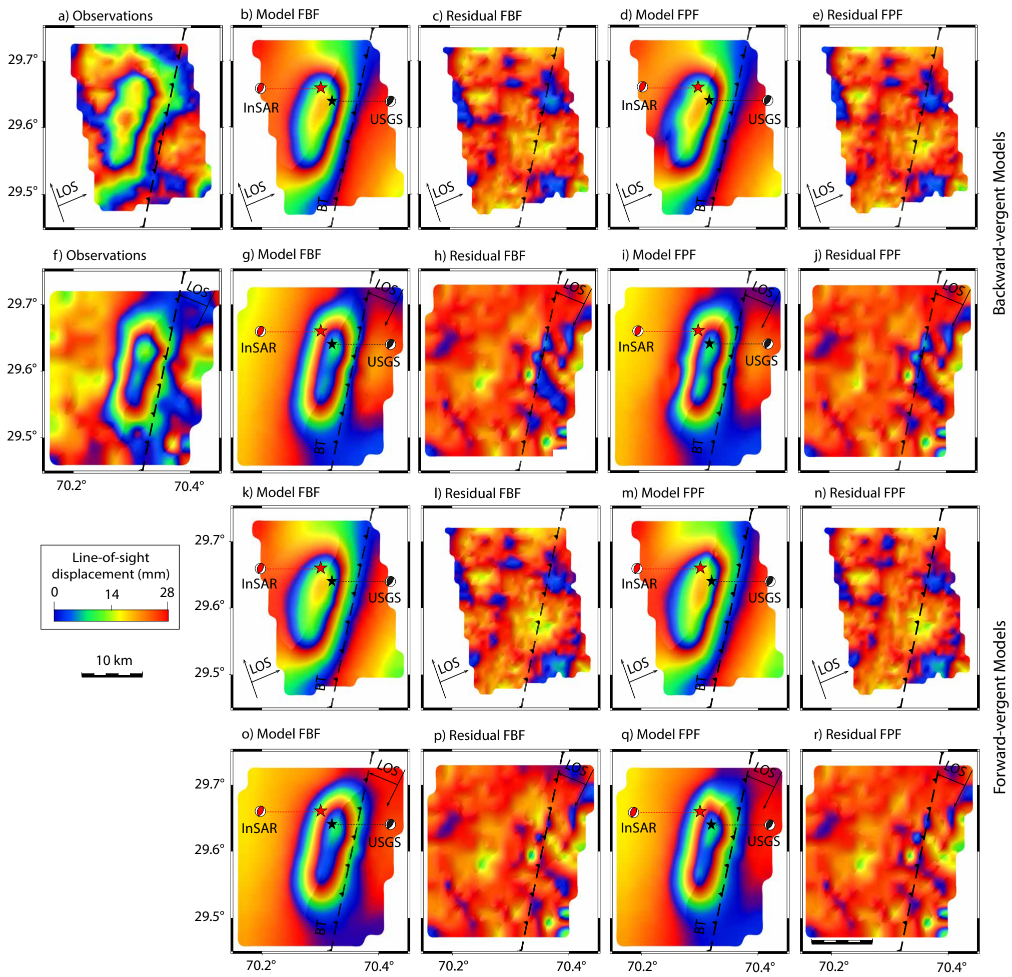

Figure S7: The FBF, and FPF model solutions a, f) ascending and descending InSAR observations, b - i) Ascending and descending backward-vergent fault-bend fold and fault-propagation fold models and residuals, k - r) Ascending and descending forward-vergent fault-bend fold and fault-propagation fold models and residuals. The maximum co-seismic slip along the LOS displacement is approximately 50 mm along with less than 2.8 mm residual for descending and ascending track respectively. Focal mechanism solution (red colored) is produced by using inverted ruptured fault parameters and focal mechanism solution (black colored) is taken from USGS.

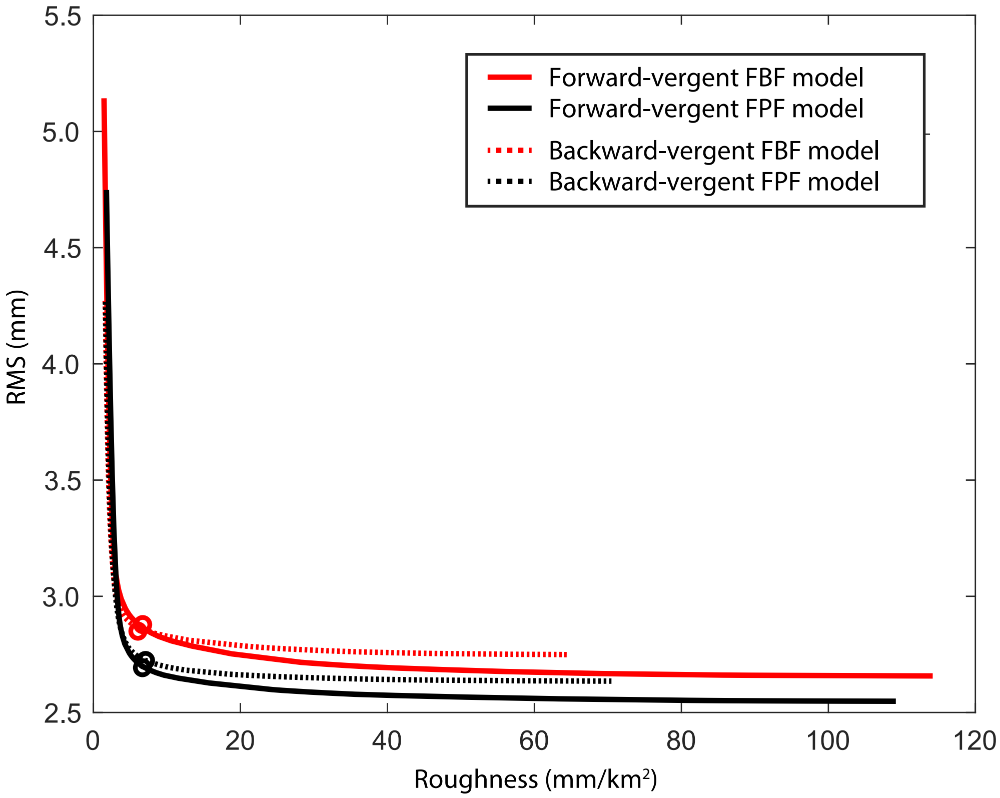

Figure S8: L-curve of RMS for foward- and backward-vergent FPF and FBF models. FPF: Fault-propagation fold, FBF: fault-bend fold agu

References

Bagnardi, M., & Hooper, A. (2018). Inversion of surface deformation data for rapid estimates of source parameters and uncertainties: A bayesian approach. *Geochemistry, Geophysics, Geosystems*, *19*(7), 2194–2211.

Baran, I., Stewart, M. P., Kampes, B. M., Perski, Z., & Lilly, P. (2003). A modification to the goldstein radar interferogram filter. *IEEE Transactions on Geoscience and Remote Sensing*, *41*(9), 2114–2118.

Chen, C., & Zebker, H. (2002). Phase unwrapping for large sar interferograms: statistical segmentation and generalized network models. *IEEE Trans. Geosci. Rem. Sens.*, *40*(8), 1709-1719.

De Zan, F., & Monti Guarnieri, A. (2006). Topsar: Terrain observation by progressive scans. *IEEE Transactions on Geoscience and Remote Sensing*, *44*(9), 2352-2360. doi: 10.1109/TGRS.2006.873853

Farr, T. G., & Kobrick, M. (2000). Shuttle radar topography mission produces a wealth of data. *Eos, Transactions American Geophysical Union*, *81*(48), 583–585.

Fukuda, J., & Johnson, K. M. (2008). A fully bayesian inversion for spatial distribution of fault slip with objective smoothing. *Bulletin of the Seismological Society of America*, *98*(3), 1128–1146.

Goldstein, R. M., & Werner, C. L. (1998). Radar interferogram filtering for geophysical applications. *Geophys. Res. Lett.*, *25*(21), 4035.

Hanssen, R. F., Weckwerth, T. M., Zebker, H. A., & Klees, R. (1999). High-resolution water vapor mapping from interferometric radar measurements. *Science*, *283*(5406), 1297–1299.

Hastings, W. K. (1970, 04). Monte Carlo sampling methods using Markov chains and their applications. *Biometrika*, *57*(1), 97-109. Retrieved from `https://doi.org/10.1093/biomet/57.1.97` doi: 10.1093/biomet/57.1.97

Jonsson, P., & Eklundh, L. (2002). Seasonality extraction by function fitting to time-series of satellite sensor data. *IEEE Transactions on Geoscience and Remote Sensing*, *40*(8), 1824-1832. doi: 10.1109/TGRS.2002.802519

Knospe, S., & Jonsson, S. (2010). Covariance estimation for dinsar surface deformation measurements in the presence of anisotropic atmospheric noise. *IEEE Transactions on Geoscience and Remote Sensing*, *48*(4), 2057-2065. doi: 10.1109/TGRS.2009.2033937

Lentas, K., Di Giacomo, D., Harris, J., & Storchak, D. A. (2019). The isc bulletin as a comprehensive source of earthquake source mechanisms. *Earth System Science Data*, *11*(2), 565–578.

Metropolis, N., Rosenbluth, A. W., Rosenbluth, M. N., Teller, A. H., & Teller, E. (1953). Equation of state calculations by fast computing machines. *The journal of chemical physics*, *21*(6), 1087–1092.

Miranda, N., Meadows, P., Type, D., & Note, T. (2015). Radiometric calibration of s-1 level-1 products generated by the s-1 ipf. *Viewed at https://sentinel. esa. int/documents/247904/685163/S1-Radiometric-Calibration-V1. 0. pdf*.

Nanjundiah, P., Barbot, S., & Wei, S. (2020). Static source properties of slow and fast earthquakes. *J. Geophys. Res.*, *125*(12), e2019JB019028. doi: 10.1029/2019JB019028

Okada, Y. (1992, April). Internal deformation due to shear and tensile faults in a half-space. *Bull. Seism. Soc. Am.*, *82*, 1018–1040.

Prats-Iraola, P., Scheiber, R., Marotti, L., Wollstadt, S., & Reigber, A. (2012). Tops interferometry with terrasar-x. *IEEE Transactions on geoscience and remote sensing*, *50*(8), 3179–3188.

Sandwell, D., Mellors, R., Tong, X., Wei, M., & Wessel, P. (2011). Gmtsar: An insar processing system based on generic mapping tools. *UC San Diego: Library – Scripps Digital Collection*.

Sansosti, E., Berardino, P., Manunta, M., Serafino, F., & Fornaro, G. (2006). Geometrical sar image registration. *IEEE Transactions on Geoscience and Remote Sensing*, *44*(10), 2861–2870.

Sathiakumar, S., Barbot, S., & Hubbard, J. (2020). Seismic cycles in fault-bend folds. *J. Geophys. Res.*, *125*(8), e2019JB018557. doi: 10.1029/2019JB018557

Simons, M., Fialko, Y., & Rivera, L. (2002). Coseismic deformation from the 1999 M_w7.1 Hector Mine, California, earthquake, as inferred from InSAR and GPS observations. *Bull. Seism. Soc. Am.*, *92*, 1390–1402.

Suppe, J. (1983). Geometry and kinematics of fault-bend folding. *Am. J. science*, *283*(7), 684–721.

Suppe, J., & Medwedeff, D. A. (1990). Geometry and kinematics of fault-propagation folding. *Eclogae Geologicae Helvetiae*, *83*(3), 409–454.

Tarantola, A. (2005). *Inverse problem theory and methods for model parameter estimation.* Philadelphia, PA, USA: Soc. Ind. App. Math.

USGS. (2020). United States Geological Survey, Earthquake Lists, Maps, and Statistics, accessed march 18, 2020. *USGS*. Retrieved from `https://doi.org/10.1093/biomet/57.1.97`

Wackernagel, H. (2003). Variogram and covariance function. In *Multivariate geo-*

statistics (pp. 50–56). Springer.

Wang, H., Liu-Zeng, J., Ng, A.-M., Ge, L., Javed, F., Long, F., … Shao, Z. (2017). Sentinel-1 observations of the 2016 menyuan earthquake: A buried reverse event linked to the left-lateral haiyuan fault. *International Journal of Applied Earth Observation and Geoinformation*, *61*, 14–21.

Yu, C., Li, Z., Penna, N. T., & Crippa, P. (2018). Generic atmospheric correction model for interferometric synthetic aperture radar observations. *Journal of Geophysical Research: Solid Earth*, *123*(10), 9202–9222.